Journal of Materials Chemistry C

ROYAL SOCIETY OF CHEMISTRY

PAPER

View Article Online
View Journal | View Issue

Cite this: J. Mater. Chem. C, 2025, 13, 14069

Generating cyan emission *via* ammonia-thermal nitridation: $Na_{18-x}Ca_{13+x}Mg_5(PO_{4-y}N_y)_{18}:Eu^{2+}$†

Nakyung Lee, [ab] Docheon Ahn [c] and Jakoah Brgoch *[ab]

Received 6th May 2025,
Accepted 5th June 2025

DOI: 10.1039/d5tc01824b

rsc.li/materials-c

As phosphor-converted LEDs continue to displace traditional light technologies, developing new down-conversion materials remains essential for improving color quality and efficiency. This research introduces a cyan-emitting oxynitride phosphor, $Na_{13.57}Ca_{17.43}Mg_5(PO_{3.75}N_{0.25})_{18}:Eu^{2+}$, synthesized through ammonolysis of the oxide, $Na_{18}Ca_{13}Mg_5(PO_4)_{18}$. The presence of nitrogen was validated using a suite of advanced analytical techniques, including Rietveld co-refinement of synchrotron X-ray and neutron diffraction data, X-ray photoelectron spectroscopy, thermogravimetric analysis, and diffuse reflectance spectroscopy. This oxynitride phosphor was subsequently shown to exhibit a broad excitation spectrum covering the UV (>350 nm) to the violet (425 nm) portions of the electromagnetic spectrum, down-converting the absorbed light, generating an efficient cyan emission. A prototype light using the new Eu^{2+}-substituted oxynitride produced a functional (daylight) white light when paired with a violet LED and commercial blue and red-emitting phosphor. This research not only introduces a promising phosphor for LED applications but also highlights a practical approach to obtain novel oxynitrides from disordered oxides with a cost-efficient synthesis method, potentially paving the way for advancements in phosphor-based lighting technologies.

1. Introduction

Enabled by the invention of the light-emitting diode (LED), phosphor-converted white LEDs (pc-wLEDs) have overtaken the lighting industry due to their superior energy efficiency, extended operating lifespan, and eco-friendly components.[1,2] Pc-wLEDs produce white light by down-converting and broadening the nearly monochromatic emission from an LED using inorganic phosphors. The most cost-effective light bulbs employ a blue-emitting (450 nm) InGaN LED chip coated with the yellow phosphor $Y_3Al_5O_{12}:Ce^{3+}$.[3] This combination of emissions produces a functional cold white light, but the lack of coverage in the cyan and red regions results in decreased color reproducibility. Today's primary solution is adding a red-emitting phosphor and a cyan-emitting phosphor to improve coverage of the visible region; however, there are few short Stokes' shift phosphors to convert blue LED light into cyan light, while the violet region always remains largely unaddressed.[4,5] An alternative strategy involves a combination of UV (~365 nm) or violet (400 nm) LED coated with a red (*e.g.*, $CaAlSiN_3:Eu^{2+}$), green (β-SiAlON:Eu^{2+} or $Lu_3Al_5O_{12}:Ce^{3+}$), and a blue ($BaMgAl_{10}O_{17}:Eu^{2+}$) phosphor to achieve continuous coverage across the entire visible spectrum.[6–9] This four-color approach can lead to higher color rendering, covering from violet to red; nevertheless, a spectral gap in the cyan region usually remains.

Designing phosphors that could close this cyan-gap begins with the strategic selection of activator ions and host materials, as these are the two components that fundamentally govern the photoluminescent properties. The activator employed in solid-state lighting is usually a rare-earth ion like Ce^{3+} and Eu^{2+} due to their selection-rule-allowed 4f ↔ 5d electronic transitions, enabling broad excitation and emission spectra.[10,11] In isolated ions, these transitions require extremely high energy (201 nm for Ce^{3+} and 294 nm for Eu^{2+});[12] however, embedding them in a host material modifies their electronic structures through two key mechanisms. The nephelauxetic effect arises when coordinating anions polarize the activator's valence electrons, increasing metal–ligand covalency.[13,14] This reduces interelectronic repulsion and stabilizes the 5d orbitals, called the centroid shift, decreasing the energy gap between 4f and 5d states. Anion polarizability follows the spectrochemical series: fluorides (weakest) < oxides < oxynitrides < nitrides < sulfides (strongest), directly correlating with observed emission red-shift as a function of the anion.[15,16] The second mechanism, crystal field splitting, occurs concurrently based on the cation site's local coordination environment, coordination number,

[a] Department of Chemistry, University of Houston, Houston, Texas 77204, USA. E-mail: jbrgoch@Central.UH.EDU
[b] Texas Center for Superconductivity, University of Houston, Houston, Texas 77204, USA
[c] PLS-II Beamline Department, Pohang Accelerator Laboratory, POSTECH, Pohang 37673, Republic of Korea

† Electronic supplementary information (ESI) available. See DOI: https://doi.org/10.1039/d5tc01824b

volume, and site symmetry.[17–20] The 5d degeneracy is lifted depending on these interactions. These two simultaneous effects cause the activator's virtual 5d orbital to shift lower in energy, moving it closer to the 4f orbital, leading to electronic transitions that can occur ideally in the visible range of the electromagnetic spectrum.

Designing new phosphors leverages this fundamental understanding of the nephelauxetic effect and crystal field splitting to achieve controllable optical properties.[21] In particular, elemental substitution to tune the visible-range emission can occur through the partial N^{3-} substitution for O^{2-}.[22,23] For example, the oxynitride β-$CaSi(O,N)_3$:Eu^{2+}, obtained by nitridation of β-$CaSiO_3$, produced a pronounced red-shifted emission ($\lambda_{em,max}$ = 618 nm) compared to its oxide counterpart ($\lambda_{em,max}$ = 472 nm).[24] This result is attributed to a stronger centroid shift and crystal field splitting stemming from the nitrogen-rich coordination environments. A similar trend is observed in the α-$SrSi(O,N)_3$:Eu^{2+} system, which emits at 550 nm and is noticeably red-shifted relative to α-$SrSiO_3$:Eu^{2+} with an emission peak at 498 nm.[24]

The discovery of oxynitrides and nitrides, such as these nitridation examples, has traditionally relied on high-temperature solid-state synthesis under high N_2 pressure or with expensive, air-sensitive metal nitride starting materials. For example, one of the most famous phosphor, β-SiAlON:Eu^{2+}, is generally synthesized at 2000 °C under 1 MPa.[7] $Ba_{3-x}Sr_x[Mg_2P_{10}N_{20}]$:$Eu^{2+}$ was synthesized under 3 GPa at 1400 °C starting from P_3N_5 and Mg_3N_2.[25] Ammonolysis, or gas reduction thermal nitridation, appears to be a more practical alternative for synthesizing oxynitrides. This process converts inexpensive oxide precursors at moderate temperatures and ambient pressure using ammonia gas as the nitrogen source. This approach has led to various oxynitrides, such as $Sr_2Si_5N_8$:Eu^{2+} and $BaSi_7N_{10}$:Eu^{2+}.[26,27] It also has successfully produced the $M^I{}_3M^{III}P_3O_9N$:Eu^{2+} (M^I = Na, K; M^{III} = Al, Ga, In) series from readily available oxide starting materials, circumventing the need for the costly and challenging to make PON precursor that was required initially.[28,29]

This report leverages the ammonolysis to produce new oxynitrides by converting a known oxide, $Na_{18}Ca_{13}Mg_5(PO_4)_{18}$, into a new oxynitride, $Na_{13.57}Ca_{17.43}Mg_5(PO_{3.75}N_{0.25})_{18}$. Substituting this phase with Eu^{2+} yields a cyan-emitting phosphor with interesting optical properties.[30] Comprehensive characterization through Rietveld co-refinement of synchrotron X-ray and neutron diffraction data revealed nitrogen substitution across most oxygen crystallographic sites, with charge compensation achieved through statistical mixing on the cation site. Additional evidence for nitrogen incorporation into the material includes X-ray photoelectron spectroscopy (XPS), thermogravimetric analysis (TGA), and diffuse reflectance spectroscopy. Eu^{2+} substitution then produces a cyan-emitting phosphor contrasting the parent oxide's UV emission, while the oxynitride also demonstrates a moderate photoluminescent quantum yield (PLQY) and reasonable temperature-dependent optical properties. A prototype pc-wLED device was constructed using the oxynitride to cover the cyan region with green and red-emitting phosphors, all excited by a violet LED to generate warm white light. This research establishes that oxynitrides with more complex structures can be developed from known oxide precursors *via* ammonolysis under moderate conditions, thereby expanding the library of viable host materials for effective phosphors.

2. Experimental procedure

2.1. Materials synthesis

The $Na_{18}Ca_{13}Mg_5(PO_4)_{18}$ host along with the oxynitride counterpart, $Na_{13.57}Ca_{17.43}Mg_5(PO_{3.75}N_{0.25})_{18}$, and the Eu^{2+} substituted phosphor series, $((Na_{13.57}Ca_{17.43})_{1-x}Eu_{31x}Mg_5(PO_{3.75}N_{0.25}))_{18}$ (x = 0.001, 0.0025, 0.005, 0.01, 0.0125) were synthesized by the solid-state reactions starting from Na_2CO_3 (Sigma-Aldrich, 96%), $CaCO_3$ (Alfa Aesar, 99.0%), MgO (Sigma-Aldrich, 99.995%), $NH_4H_2PO_4$ (Acros Organics, 99.9%), and Eu_2O_3 (Alfa Aesar, 99.99%). Each component was weighed out in the appropriate stoichiometric ratio. The mixed starting reagents were ground in an agate mortar and pestle using acetone as a wet medium and further milled for 30 min in a high-energy ball mill (Spex 800 M Mixer/Mill). The mixtures were pressed into a 6 mm diameter pellet and placed on a bed of sacrificial powder in a boron nitride crucible. All pellets were heated to 800 °C for 12 h with a heating and cooling rate of 3 °C min^{-1}. The $Na_{18}Ca_{13}Mg_5(PO_4)_{18}$ oxide samples were synthesized under flowing 5% H_2/95% Ar gas, whereas the oxynitride compositions were reacted under flowing dehydrated NH_3 gas. The NH_3 gas acted as a reducing agent to convert Eu^{3+} into Eu^{2+} and a nitrogen source to convert the oxide into an oxynitride.

2.2. Characterization

The polycrystalline products were first analyzed for phase purity using powder X-ray diffraction on an X'Pert PANalytical Empyrean 3 equipped with Cu Kα radiation (λ = 1.54056 Å). The oxide and oxynitride host crystal structures were subsequently analyzed with high-resolution synchrotron powder X-ray diffraction data collected on 9B beamline of PLS-II. Neutron powder diffraction was also collected using the Spallation Neutron Source (SNS-POWGEN) at Oak Ridge National Laboratory.[31] Both sets of data were collected at 100 K. The structures were then solved through a combined Rietveld refinement process performed using the general structural analysis system II (GSAS-II) software.[32] The background for each diffractogram was described using a Chebyshev-1 function, and the peak shapes were modeled using a pseudo-Voigt function. The unit cell parameters were initially refined using the Le Bail method, which only used synchrotron X-ray diffraction data. Subsequently, atomic positions and atomic displacement parameters were independently refined *via* the Rietveld method, simultaneously incorporating both synchrotron X-ray and neutron diffraction datasets. Occupancies were finally refined using only neutron scattering data, with constraints set when refining the oxynitride to ensure charge balance between the cations and anions. The final crystal structure was visualized using VESTA.[33]

X-ray photoelectron spectra were collected using a physical electronics PHI 5700 ESCA System. Thermogravimetric analysis and differential scanning calorimetry were measured using TA Instruments TGA 2050 up to 950 °C with a heating rate of 5 °C min^{-1}. Diffuse reflectance spectra were collected using a JASCO V-770 UV-Visible spectrophotometer.

Photoluminescence measurements involved mixing the polycrystalline products in an optically transparent silicon epoxy (United Adhesives Inc., OP 4036) and depositing the combination onto a quartz slide (Chemglass). Photoluminescent excitation and emission and temperature-dependent luminescence measurements were obtained using a PTI fluorescence spectrophotometer with a 75 W xenon arc lamp for excitation. A Janis cryostat VPF-100 was employed to establish a temperature-controlled environment from 80 K to 640 K. The PLQY was determined following the method of de Mello *et al.*, using a Spectralon-coated integrating sphere (150 mm diameter, Labsphere).[34] Luminescent measurements at 15 K (λ_{ex} = 364 nm and 405 nm) were conducted in a closed-cycle refrigerator system by CRYO Industries of America, Inc. The sample was measured by adhering the material to the surface of a copper cold finger in a vacuum. The laser power was maintained at 0.1 mW, and the luminescence spectrum was collected using an iHR 320 spectrometer equipped with a thermoelectric-cooled Synapse charge-coupled device.

2.3. Prototype construction

Two prototype devices were constructed. The first was prepared using commercially available β-SiAlON:Eu^{2+} as the green phosphor, $BaMgAl_{10}O_{17}$:Eu^{2+} as the blue phosphor, and $CaAlSiN_3$:Eu^{2+} as the red in a 1.5 : 10 : 1 ratio (Device RGB). The second involved using $(Na_{13.57}Ca_{17.43})_{0.995}$ $Eu_{0.155}Mg_5(PO_{3.75}N_{0.25})_{18}$ as the cyan component, commercially available $BaMgAl_{10}O_{17}$:Eu^{2+} as the blue phosphor, and $CaAlSiN_3$:Eu^{2+} as the red phosphor in a 33 : 3.3 : 1 ratio (Device RCyB). The three phosphors were ground in an agate mortar and mixed in optically transparent silicone resin in both cases. The resins were formed into phosphor caps using a custom brass mold. These caps were placed on top of a 395 nm emitting LED driven by a forward bias of 20 mA. The white light spectra of the prototypes were collected and characterized using an Avasphere-5-IRRAD spectrophotometer and AvaSoft 8 software.

3. Results and discussion

3.1. Nitridation of $Na_{18}Ca_{13}Mg_5(PO_4)_{18}$

The host structure, $Na_{18}Ca_{13}Mg_5(PO_4)_{18}$, was originally identified as a single crystal, which emerged as a byproduct during the synthesis of $Na_2CaMg(PO_4)_2$.[30] In this prior study, a single crystal was picked from a product that was synthesized using $NaPO_3$, CaO, and MgO at an initial temperature of 800 °C followed by gradual cooling to 500 °C at a rate of 5 °C h^{-1}. Na_2MoO_4 was used as a flux to assist single crystal growth, which could be washed away with water. Single crystal X-ray diffraction revealed the disordered structure of $Na_{18}Ca_{13}Mg_5(PO_4)_{18}$ crystallized in space group $R\bar{3}m$ (no. 166). This study successfully re-synthesized the target materials as a polycrystalline product through solid-state synthesis at 800 °C starting from oxide powders. The sample's phase purity and structural characteristics were determined through combined Rietveld refinement of powder synchrotron X-ray and neutron diffraction data, starting from the reference pattern (ICSD#408372) corresponding to the originally published crystal structure. The combined refinement using X-ray and neutron scattering is advantageous for accurate structure determination due to their complementary information. Powder X-ray diffraction provides accurate unit cell information and is good at distinguishing the positions of heavier atoms, whereas neutron scattering is able to identify the location of the lighter atoms, provide more reliable information on the atomic displacement parameters, and most importantly, distinguish nitrogen from oxygen given their neutron scattering cross-sections (N: 11.51 barn, O: 4.232 barn), which is not possible with X-ray diffraction.[35] The refined diffractograms and crystal structure are shown in Fig. 1. The final refinement statistics, lattice parameters, and atomic positions and displacement parameters are summarized in Tables S1 and S2 (ESI†).

This crystal structure contains ten crystallographically independent cation sites, several exhibiting statistical disorder (site mixing) while others having partial occupancies (Fig. S1, ESI†).

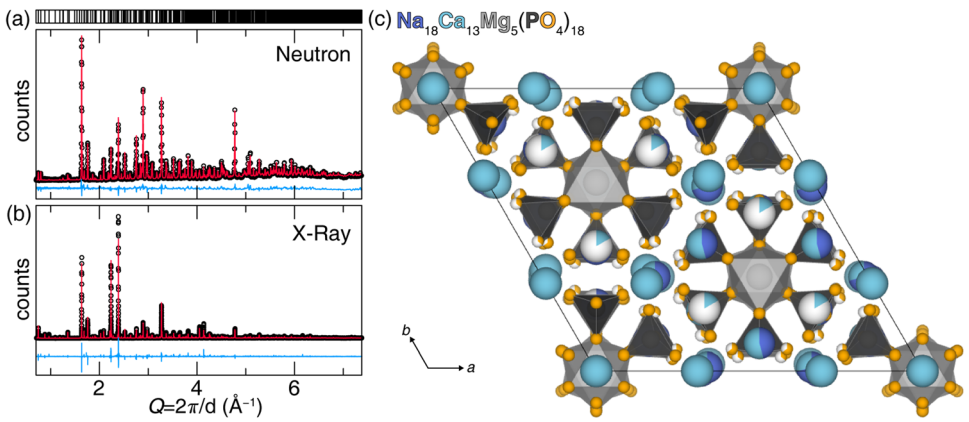

Fig. 1 Rietveld Co-refinement using (a) neutron diffractogram and (b) synchrotron powder X-ray diffractogram of $Na_{18}Ca_{13}Mg_5(PO_4)_{18}$ host started from ICSD #408372 and (b) the resulting refined structure.

The bonding lengths (Ca–O = 3.27 Å, Ca–N = 3.0 Å, Na–O = 2.96 Å, and Na–N = 3.13 Å) are consistent with similar published structures, although varying degrees of polyhedron distortion are observed here. Among the seven cation sites only two, [Ca(1)O_6] and [Na(5)O_7], are fully ordered. Three sites are influenced by partial occupancies of the O(9) and O(10), which are split into six different sites. As a result, [Ca(2)O_8] and the disordered site, [M(3)O_8] (M = Na^+/Ca^{2+}), are each divided into two crystallographic sites with the same coordination number but slightly different degrees of distortion. The second disordered site of M(4) is more complex, connecting to O(9) generating [M(4)O_{10}] whereas O(10) leads to a [M(4)O_8]. Following structure refinement, the occupancies of the highly disordered sites [Ca(6)O_{11}] and [Na(6)O_8] were determined to be 16.8(6)% and 83.2(6)%, respectively, slightly deviated from the initial values of 15% and 85% reported in ICSD#408372.

This specific disorder is why the phosphate was selected for nitridation, because the disorder between Na^+ and Ca^{2+} can compensate for the charge difference when partially substituting O^{2-} with N^{3-}. The oxynitride synthesis employed flowing NH_3 as the nitrogen source during the solid-state synthesis. A combined Rietveld X-ray and neutron diffraction data refinement again confirmed the product's purity and structure. The charge compensation was accommodated by varying the Na^+/Ca^{2+} ratio as a function of O^{2-}/N^{3-} content. The co-refined data, with a weighted *R*-factor (w*R*) of 8.27%, supports the absence of significant impurities and highlights strong agreement between the collected data and the structure model, as illustrated in Fig. 2a and b. The refined structure is shown in Fig. 2c. Detailed refinement statistics and the refined atomic positions and displacement factors are provided Tables S3 and S4 (ESI†). The refined composition of the oxynitride host, $Na_{13.57(2)}Ca_{17.43(2)}Mg_5P_{18}O_{67.54(3)}N_{4.46(3)}$, exhibited increased Ca^{2+} compared to the oxide composition, $Na_{18}Ca_{13}Mg_5(PO_4)_{18}$. This altered Na^+/Ca^{2+} ratio charge compensates (within standard deviation) for the additional negative charge stemming from the structure's incorporation of N^{3-}.

Nitrogen's location in the structural backbone as well as each coordination polyhedron, are illustrated in Fig. 3. During the refinement process, O(2), O(7), and O(8) were found to remain the only purely oxygen positions, whereas O(9) was entirely replaced by N^{3-}, becoming N(9) in the refined oxynitride structure. While this nitridation preserves the original coordination number and connectivity of the 10 cation sites, the extent of nitridation varies significantly among the [Ca(2)O_8], [M(3)O_8], and [M(4)O_{10}/O_8]. The Ca(6) and Na(6) sites exhibit 26.9(8)% and 73.1(8)% occupancy, respectively. There is no clear pattern in the site preference for nitrogen incorporation in the new oxynitride product.

Rietveld refinement is a powerful tool for analyzing the structures of polycrystalline materials. Yet, the complexity of $Na_{13.57}Ca_{17.43}Mg_5(PO_{3.75}N_{0.25})_{18}$, with its numerous anion positions and statistical mixing on nearly every crystallographic site, necessitated additional measurements to confirm the presence of nitrogen. XPS analysis was conducted successively to corroborate the presence of N^{3-}. The survey spectra for both the oxide and oxynitride hosts revealed only the presence of loaded starting elements, indicating no contamination during synthesis (Fig. 4a). The subsequent collection of high-resolution (HRES) spectra to improve the signal-to-noise ratio, as shown in the inset, supported the absence of any signal from N 1s in the sample synthesized under 5% H_2/95% Ar, whereas a clear N 1s peak is present in the oxynitride, substantiating the presence of nitrogen.

Several thermal analysis experiments were performed to support nitrogen in the sample. First, a simple experiment exploits the fact that oxynitrides should oxidize at high temperatures. Therefore, the sample reacted under ammonia to form the oxynitride was subsequently heated at 1000 °C in air for 12 hours to oxidize the sample. Powder X-ray diffraction and Le Bail refinement revealed that the oxynitride's post-oxidation unit cell volume decreased from 4677.1(5) $Å^3$ (sample pre-heating) to 4632.1(5) $Å^3$ (sample post-heating). The unit cell volume of the post-heating sample is nearly the same as the phosphate synthesized under H_2/Ar gas (4641.0(4) $Å^3$; Fig. S2a and Table S5, ESI†). Additional XPS analysis shows that the N 1s signal in the pre-heated sample disappears in the post-heated sample, supporting the change in lattice parameters stems

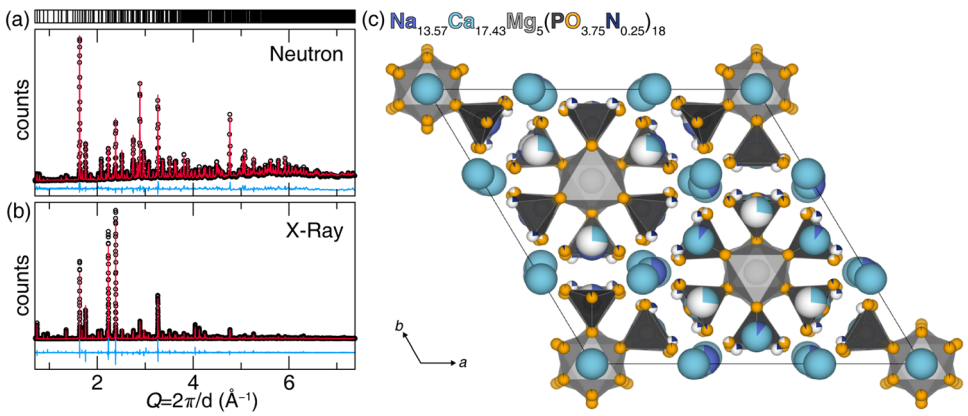

Fig. 2 Rietveld Co-refinement using (a) neutron diffraction and (b) synchrotron PXRD of oxynitride $Na_{13.57}Ca_{17.43}Mg_5(PO_{3.75}N_{0.25})_{18}$ host started from ICSD #408372. (c) Refined structure maintains the disorder and partial occupancies across Na^+/Ca^{2+} cation sites.

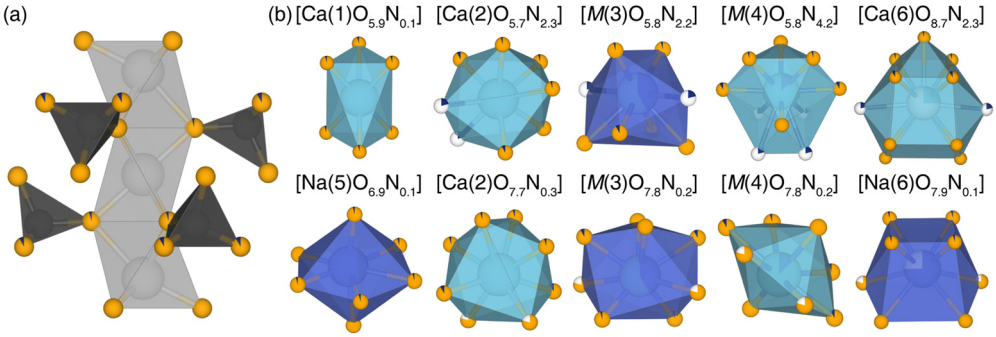

Fig. 3 (a) The octahedral magnesium oxide and tetrahedral phosphate backbone and (b) 10 cation sites incorporating nitrogen in the refined structure of oxynitride $Na_{13.57}Ca_{17.43}Mg_5(PO_{3.75}N_{0.25})_{18}$ host. M = Na^+/Ca^{2+}.

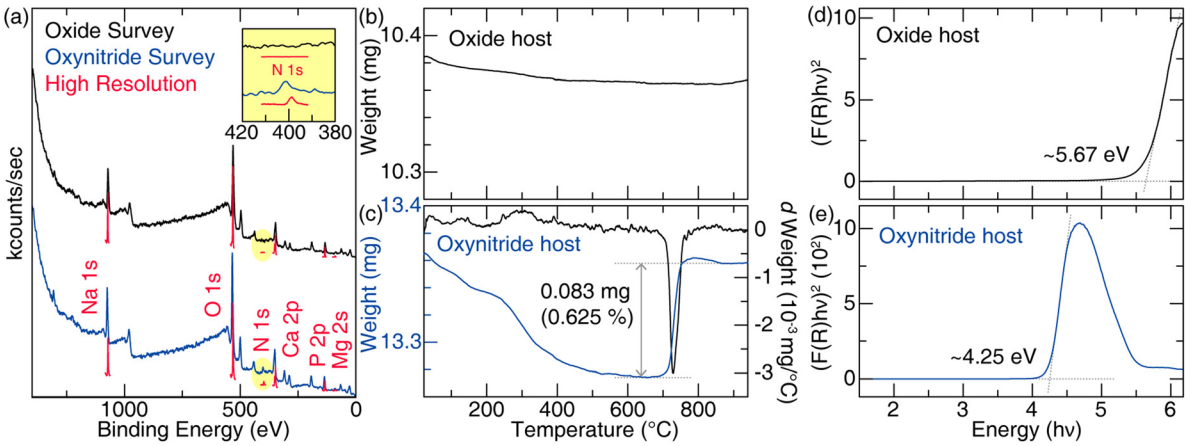

Fig. 4 (a) XPS spectra for the oxide $Na_{18}Ca_{13}Mg_5(PO_4)_{18}$ and oxynitride $Na_{13.75}Ca_{17.43}Mg_5(PO_{3.75}N_{0.25})_{18}$ host with an inset highlighting the N 1s region. TGA results for (b) the oxide and (c) the oxynitride hosts, with simultaneous DSC measurement of the oxynitride. Tauc plots from diffuse reflectance spectra of (d) oxide and (e) oxynitride hosts for bandgap determination.

from nitrogen loss (Fig. S2b, ESI†). A more quantitative analysis was performed by thermogravimetric analysis (TGA) to quantify the total nitrogen content based on weight change, with only minor variations attributed to possible decomposition of residual starting materials or side products below the detection limit of powder X-ray diffraction (Fig. 4b). The oxynitride sample (Fig. 4c) had an initial sample weight of 13.365 mg that decreased to 13.275 mg at 612 °C and 686 °C, before a dramatic and sharp increase in the sample weight to 13.358 mg at 727 °C corresponding well to the oxidation of $Na_{13.75}Ca_{17.48}Mg_5(PO_{3.75}N_{0.25})_{18}$ to $Na_{13.75}Ca_{17.48}Mg_5(PO_4)_{18}$. Differential scanning calorimetry (DSC) was simultaneously measured for the oxynitride to oxide conversion, showing a similar change in the sample. This comprehensive characterization data provides strong evidence for the presence of nitrogen in the sample, agreeing with the neutron scattering refinement.

Finally, measuring the bandgap (E_g) using diffuse reflectance spectroscopy of the oxide and oxynitride shows that incorporating nitrogen, given that the electronegativity of N^{3-} (χ_N = 3.04) is lower than O^{2-} (χ_O = 3.44), reduces the E_g.[36] Here, the band gap can be estimated by transforming the diffuse reflectance data into absorption using the Kubelka–Munk function provided in eqn (1),

$$F(R_\infty) \equiv \frac{K}{S} = \frac{(1-R_\infty)^2}{2R_\infty} \quad (1)$$

where R_∞ is the diffuse reflectance, K is the absorption coefficient, and S is the scattering coefficient.[37] Assuming perfect diffusion of incident radiation, K equals to 2α (linear absorption coefficient), and S remains constant with wavelength. The Tauc relation was subsequently applied to calculate E_g following eqn (2),

$$[F(R_\infty)h\nu]^\alpha = A(h\nu - E_g) \quad (2)$$

where ν is light frequency, and A is the proportionality constant. Both the $Na_{18}Ca_{13}Mg_5(PO_4)_{18}$ and $Na_{13.57}Ca_{17.43}Mg_5(PO_{3.75}N_{0.25})_{18}$ data were best described when $\alpha = 2$, indicating a direct band gap, while the E_g values were calculated to be 5.67 eV and 4.25 eV, respectively (Fig. 4d and e). The smaller bandgap for the oxynitride compared to its oxide counterpart is expected based on the more covalent bonding present in the oxynitride. It is also observed in literature; for example, a perovskite $LaTiO_xN_y$ has an E_g of around 2.30 eV, while $LaTiO_3$ shows an E_g of 3.26 eV.[38] This result aligns with predictions,

qualitatively indicating the presence of N^{3-}. In either case, the large bandgaps suggest that these host structures are promising candidates to be substituted with a rare-earth to produce a phosphor.

3.2. Photoluminescent properties of Eu^{2+} in $Na_{13.57}Ca_{17.43}Mg_5(PO_{3.75}N_{0.25})_{18}$

The evidence of nitridation is more pronounced in the photoluminescence of these materials once Eu^{2+} is substituted in the host. Phosphors containing one atomic percent of Eu^{2+} substituted for Na^+ and Ca^{2+} were synthesized for preliminary photoluminescence excitation and emission measurements. The oxide phosphor exhibited a UV range emission with $\lambda_{ex,max}$ = 323 nm, rendering it unsuitable for practical applications (Fig. 5a). In contrast, the oxynitride phosphor displayed bright cyan color emission with a broad excitation range spanning 365 nm to 400 nm (Fig. 5b). The red-shifted emission can be justified by nitrogen's stronger nephelauxetic effect. The broader excitation and emission spectra can be further attributed to the large and diverse number of cation sites with varying numbers of nitrogen atoms that could be substituted with Eu^{2+}. For instance, $[Ca(2)O_{5.7}N_{2.3}]$ and $[Ca(2)O_{7.7}N_{0.3}]$ possess similar distorted 8-coordinate sites, but the additional N^{3-} atoms in the former site further red-shift its emission compared to the latter. To *dig* deeper into these findings, an optimization of Eu^{2+} concentration was subsequently conducted.

The purity of five oxynitride phosphors with varying Eu^{2+} concentrations following the general formula, $(Na_{13.57}Ca_{17.43})_{1-x}Eu_{31x}Mg_5(PO_{3.75}N_{0.25})_{18}$ (x = 0.001, 0.0025, 0.005, 0.01, 0.0125), were synthesized as pure phase products based on the laboratory powder X-ray diffractograms (Fig. 6a). The unit-cell volume exhibited a linear increase with Eu^{2+} concentration due to larger ionic radii of Eu^{2+} compared to Na^+ and Ca^{2+} (*e.g.*, for 8-coordination, r_{Eu} = 1.25, r_{Na} = 1.18, and r_{Ca} = 1.12) adhering to Vegard's law (Fig. 6b).[39,40] The refined lattice parameters and refinement statistics are provided in Table S6 (ESI†). Considering the wide excitation range, the emission spectra were measured under 365 nm and 400 nm. Emission spectra under 365 nm excitation showed a slight red shift from 490 nm (x = 0.001) to 498 nm (x = 0.0125), while 400 nm excitation produced narrower, more red-shifted peaks from 498 nm (x = 0.001) to 502 nm (x = 0.0125) (Fig. S3, ESI†). Photoluminescence quantum yield (PLQY) measurements revealed higher values under 365 nm excitation, peaking at 55(3)% for x = 0.005, compared to 33.5(1)% under 400 nm excitation for the same composition (Fig. 6c). These PLQY values indicate a potential for applications pending further optimization and post-processing. For example, previous studies have shown that carbon coating on $BaMgAl_{10}O_{17}:Eu^{2+}$ can improve PLQY by reducing surface defects and preventing Eu^{2+} oxidation.[41] Different starting materials can also improve quantum yield, such as in the case of EuB_6 instead of Eu_2O_3 for $CaAlSiN_3:Eu^{2+}$.[42] Similarly, the PLQY of the NIR phosphor $CaO:Eu^{2+}$ was enhanced from 17.9% to 54.7% using carbon paper to promote the reduction of Eu^{3+} to Eu^{2+}, while the addition of GeO_2 was found to reduce oxygen vacancies.[43] Although 365 nm excitation yielded superior PLQY, 400 nm was prioritized for further measurement due to its relevance with commercial violet LEDs. The x = 0.005 concentration was selected for photoluminescence analysis because it had the highest quantum yield.

The selected sample $(Na_{13.57}Ca_{17.43})_{0.995}Eu_{0.155}Mg_5(PO_{3.75}N_{0.25})_{18}$ exhibits an emission peak at 500 nm with the full-width-at-the-half-maximum (fwhm) of 90 nm (3600 cm^{-1}) (Fig. 7a). This selected sample shows narrower and red-shifted emission spectra across the wider excitation range (330 nm to 410 nm), with the emission peak shifting from 484 nm to 503 nm, as shown in Fig. S4a (ESI†). The excitation spectra for different emission wavelengths reveal significant changes in peak position and shape (Fig. S4b, ESI†). For the 450 nm emission, a broad excitation peak appears at 350 nm. As the monitored emission wavelength increases to 530 nm, three changes occur: the 300 nm shoulder intensity decreases, the peak shifts to 375 nm, and the intensity around 400 nm increases. These observations support the presence of multiple Eu^{2+} sites within the host lattice, each contributing distinctly to the phosphor's luminescence properties.

Low-temperature (15 K) emission measurements were conducted to deconvolute the complex photoluminescence arising from the sample's ten crystallographically independent cation sites. At extremely low temperatures, the thermal vibration of the phosphor is limited, which reduces spectral broadening and allows for a more precise analysis of emission peak positions from each cation site. Under 405 nm laser excitation at 15 K, the emission spectrum reveals a peak at 520 nm that is red-shifted relative to the room temperature peak position, which can be attributed to increased crystal field splitting due to the decreased unit cell volume as a function of temperature (Fig. 7b). Gaussian deconvolution

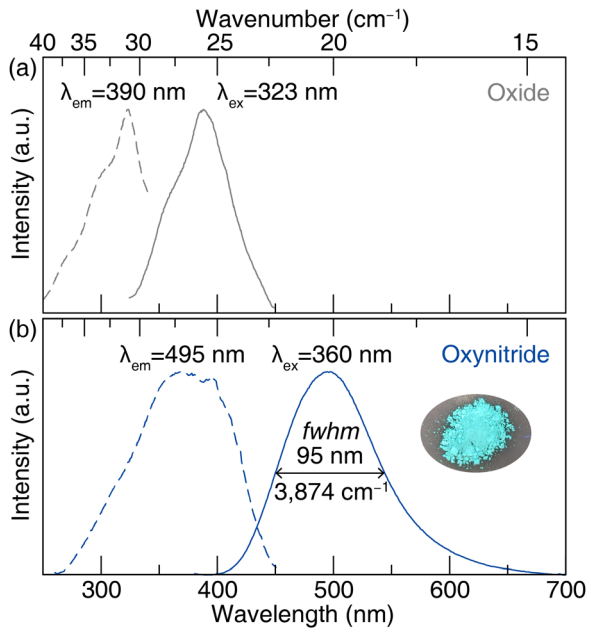

Fig. 5 Photoluminescence excitation and emission of (a) $(Na_{18}Ca_{13})_{0.99}Eu_{0.31}Mg_5(PO_4)_{18}$ and (b) $(Na_{13.57}Ca_{17.43})_{0.99}Eu_{0.31}Mg_5(PO_{3.75}N_{0.25})_{18}$.

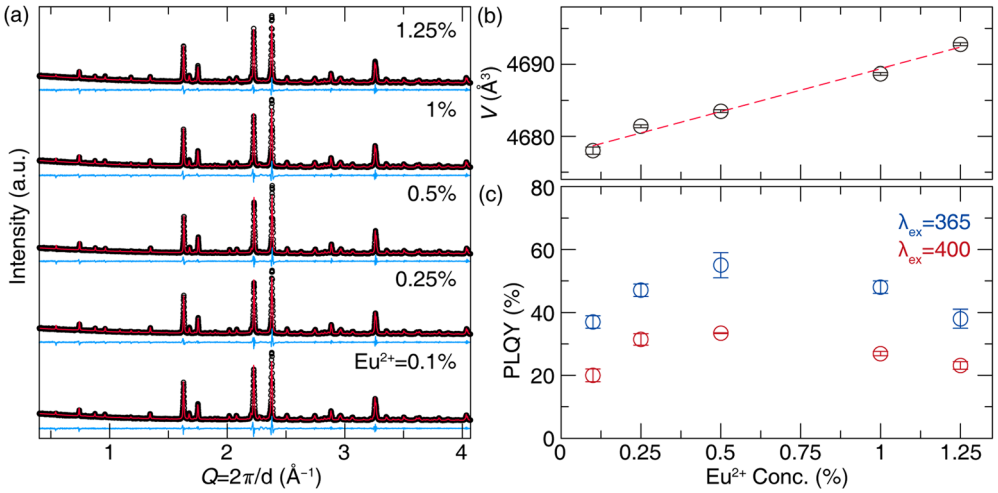

Fig. 6 (a) Le Bail refinements of $(Na_{13.57}Ca_{17.43})_{1-x}Eu_{31x}Mg_5(PO_{3.75}N_{0.25})_{18}$ started from ICSD #408372 (b) calculated volumes of the solid solution demonstrate a linear increase according to the Eu^{2+} concentration. (c) Room-temperature PLQY of the solid solution shows that x = 0.005 is the optimized concentration.

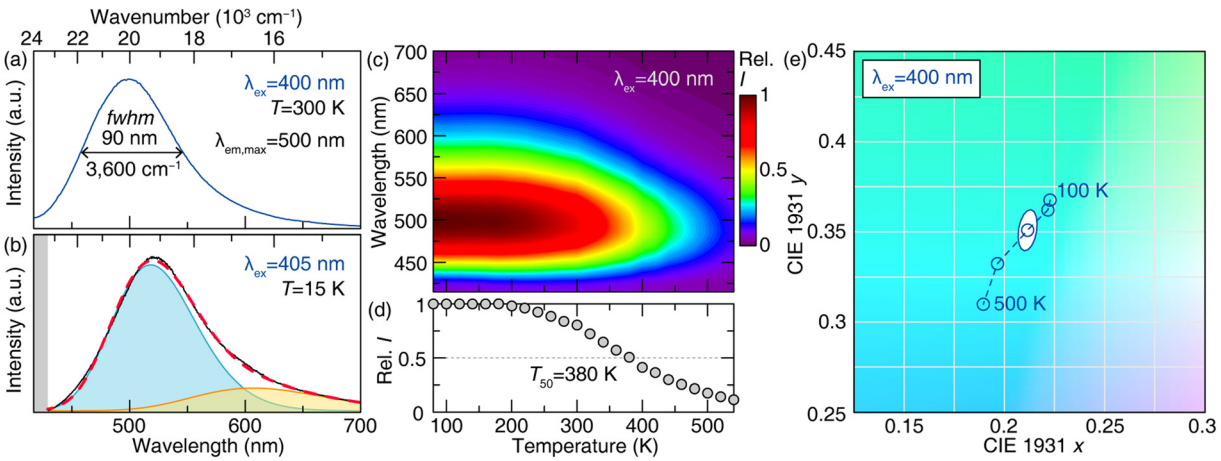

Fig. 7 Photoluminescence emission of $(Na_{13.57}Ca_{17.43})_{0.995}Eu_{0.155}Mg_5(PO_{3.75}N_{0.25})_{18}$ at room temperature (a) under 400 nm excitation and (b) the emission spectrum under 405 nm excitation at 15 K with the emission peak deconvoluted to distinguish two groups of substitution sites. (c) The contour plot of photoluminescence temperature-dependent emission at 400 nm excitation and (d) the change in the integrated intensity. (e) Changes in chromaticity in CIE 1976 space at 400 nm excitation. The white oval shapes present a 3-step MacAdam ellipse at 300 K.

was performed after converting the wavelength scale to energy (eV) using the Jacobian conversion.[44] Although there are ten cation sites, deconvolution was limited to two peaks to avoid overfitting. The resulting two deconvoluted peaks, centered at 518 nm and 607 nm, suggest two different types of similar polyhedral environments. Unfortunately, the complexity of the structure limits any further interpretation of these data beyond the indication of two groups of polyhedral environments.

The operating temperature of a commercial LED package, approximately 425 K, necessitates a thermally robust phosphor emission so the down-conversion process can withstand any thermal quenching processes.[45] Chromatic stability under increasing temperatures is also critical for maintaining a consistent hue in practical applications. Thermal stability was analyzed by determining the thermal quenching temperature (T_{50}), where the relative emission intensity drops by 50% by measuring from 80 K to 550 K. Temperature-dependent emission measurements for $(Na_{13.57}Ca_{17.43})_{0.995}Eu_{0.155}Mg_5(PO_{3.75}N_{0.25})_{18}$ revealed a slight peak position change from 500 nm to 480 nm along the increasing temperature (Fig. 7c). The integrated intensity of each spectrum showed thermal stability under 400 nm excitation with T_{50} = 380 K (Fig. 7d). Chromatic stability of the oxynitride with 0.5% Eu^{2+} was also assessed using emission spectra from 100 K to 500 K in 100 K steps, with coordinates plotted in CIE 1976$u'v'$ space and a 3-step MacAdam ellipse shown as the white circle. The MacAdam ellipse represents the possible range (change) in color before it is distinguishable to the average human eye from a reference color (Fig. 7e).[46] To quantify the emission color change, the

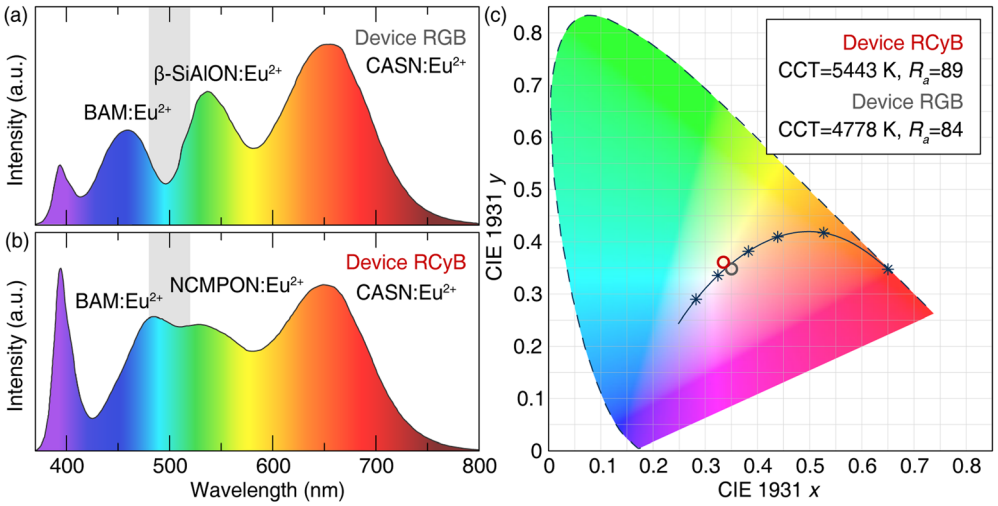

Fig. 8 The emission spectrum of a device constructed of (a) a red-green-blue phosphor (RGB) based white pc-LED made using $BaMgAl_{10}O_{17}:Eu^{2+}$ (BAM:Eu^{2+}), β-SiAlON:Eu^{2+}, and $CaAlSiN_3:Eu^{2+}$ (CASN:Eu^{2+}), and (b) a red-cyan-blue (RCyB) based white pc-LED made using BAM:Eu^{2+}, $(Na_{13.57}Ca_{17.43})_{0.995}Eu_{0.155}Mg_5(PO_{3.75}N_{0.25})_{18}$ (NCMPON:Eu^{2+}), and $CaAlSiN_3:Eu^{2+}$ with 395 nm LED. The gray area reflects cyan gap (480 nm to 520 nm) (c) The CIE coordinates of these devices demonstrate the production of daylight quality white light.

distance between the color coordinates at 300 K $\left(u'_{\text{init.}}, v'_{\text{init.}}\right)$ and the average coordinates across five temperatures $\left(u'_{\text{avg.}}, v'_{\text{avg.}}\right)$ was calculated using eqn (3).[47]

$$\Delta u'\Delta v' = \sqrt{\left(u'_{\text{avg.}} - u'_{\text{init.}}\right)^2 + \left(v'_{\text{avg.}} - v'_{\text{init.}}\right)^2} \qquad (3)$$

The calculated $\Delta u'\Delta v'$ value is 0.0071 for 400 nm excitation. While these fall short of the most recent U.S. Department of Energy goals, further tuning of the composition may yield performance gains.

3.3. pc-wLED device fabrication with $(Na_{13.57}Ca_{17.43})_{0.995}Eu_{0.155}Mg_5(PO_{3.75}N_{0.25})_{18}$

The performance of the $(Na_{13.57}Ca_{17.43})_{0.995}Eu_{0.155}Mg_5(PO_{3.75}N_{0.25})_{18}$ phosphor was finally evaluated by creating a prototype device and comparing it to the green phosphor β-SiAlON:Eu^{2+}. For the comparison group, Device RGB was first assembled using commercial blue ($BaMgAl_{10}O_{17}:Eu^{2+}$), green (β-SiAlON:$Eu^{2+}$), and red ($CaAlSiN_3:Eu^{2+}$) phosphors in a silicon mold to produce a phosphor cap placed on top of a violet-emitting LED (λ_{ex} = 395 nm) driven at 20 mA. The resulting photoluminescence spectrum exhibited a pronounced cyan gap between 480 nm and 520 nm, as illustrated in Fig. 8a. Subsequently, the β-SiAlON:Eu^{2+} in the RGB device was replaced with the cyan-emitting $(Na_{13.57}Ca_{17.43})_{0.995}Eu_{0.155}Mg_5(PO_{3.75}N_{0.25})_{18}$ to create a red-cyan-blue (RCyB) based device. The emission spectrum of Device RCyB under identical conditions effectively bridged the cyan gap and covered the full visible region of the electromagnetic spectrum, as desired (Fig. 8b). Plotting the color point of both devices on 1931 CIE coordinates shows that the lights fall near the Planckian locus with (x, y) = (0.3505, 0.3480) for Device RGB and (x, y) = (0.3341, 0.3616) for Device RCyB (Fig. 8c). While both achieved daylight white lighting with color correlated temperature (CCT) of 4778 K for Device RGB and 5443 K for Device RCyB, Device RCyB demonstrated superior color quality, elevating the color rendering index (CRI, R_a) from 84 to 89 due to enhanced cyan-yellow coverage.

4. Conclusion

This study presents a novel Eu^{2+}-activated oxynitride phosphor, $(Na_{13.57}Ca_{17.43})_{0.995}Eu_{0.155}Mg_5(PO_{3.75}N_{0.25})_{18}$, synthesized through ammonolysis of $Na_{18}Ca_{13}Mg_5(PO_4)_{18}$. Comprehensive characterization using synchrotron X-ray and neutron diffraction, along with spectroscopic and thermal analyses, confirmed the successful incorporation of nitrogen into the host lattice. Compared to its oxide counterpart, the resulting phosphor exhibits useful optical properties with a bright cyan emission under a broad excitation range and a moderate photoluminescent quantum yield of 33.5(1)% under 400 nm. This oxynitride phosphor further demonstrates moderate thermal stability. Fabricating an LED device with $(Na_{13.57}Ca_{17.43})_{0.995}Eu_{0.155}Mg_5(PO_{3.75}N_{0.25})_{18}$ could reproduce daylight with a high CRI value of 89. In contrast, a device based on β-SiAlON:Eu^{2+} reproduced daylight with a slightly lower CRI of 84, mainly due to the absence of cyan emission, demonstrating the need for making phosphors that cover this portion of the visible spectrum.

Indeed, significant advancements in cyan-emitting phosphors have been achieved over the past decade, with notable materials demonstrating distinct advantages. For example, $NaMgBO_3:Ce^{3+}$ exhibits high-efficiency blue-cyan emission at 480 nm (fwhm = 102 nm), boasting an exceptional PLQY of 97% and outstanding thermal stability, with 90% intensity retention at 500 K and zero chromaticity drift.[48] However, its 370 nm excitation wavelength limits compatibility to standard UV LED sources. $Na_{0.5}K_{0.5}Li_3SiO_4:Eu^{2+}$ features an ultranarrow cyan peak at 486 nm (fwhm = 20.7 nm) from its UCr_4C_4-type cubic

structure, achieving 76% PLQY under 400 nm excitation.[4] This phosphor maintains functionality under 450 nm blue LEDs and can be combined with YAG:Ce^{3+} and K_2SiF_6:Mn^{4+} to achieve an impressive CRI of 95. While the nitridated phosphor reported here, $(Na_{13.57}Ca_{17.43})_{0.995}Eu_{0.155}$ $Mg_5(PO_{3.75}N_{0.25})_{18}$, does not quite achieve the same metrics as these two materials to varying degrees, the material still effectively covers the cyan gap. Most importantly, this work demonstrates a synthetic approach that opens avenues for discovering novel oxynitride phosphors by converting known oxide phases, potentially advancing the development of more efficient and versatile materials for next-generation LED lighting.

Data availability

The data supporting this article have been included as part of the ESI.†

Conflicts of interest

The authors declare no competing financial interest.

Acknowledgements

This work was supported by the National Science Foundation (DMR-2349319) and the Welch Foundation (E-2181). The authors thank Dr Boris Makarenco for assisting with XPS measurement, Dr Tatyana Makarenco for TGA measurement, and Prof. Jiming Bao and Ms Chengzhen Qin for performing photoluminescent emission measurement at 15 K.

References

1 P. Pust, P. J. Schmidt and W. Schnick, A Revolution in Lighting, *Nat. Mater.*, 2015, **14**(5), 454–458, DOI: 10.1038/nmat4270.
2 N. C. George, K. A. Denault and R. Seshadri, Phosphors for Solid-State White Lighting, *Annu. Rev. Mater. Res.*, 2013, **43**, 481–501, DOI: 10.1146/annurev-matsci-073012-125702.
3 X. He, X. Liu, R. Li, B. Yang, K. Yu, M. Zeng and R. Yu, Effects of Local Structure of Ce^{3+} Ions on Luminescent Properties of $Y_3Al_5O_{12}$:Ce Nanoparticles, *Sci. Rep.*, 2016, **6**(1), 22238, DOI: 10.1038/srep22238.
4 M. Zhao, H. Liao, M. S. Molokeev, Y. Zhou, Q. Zhang, Q. Liu and Z. Xia, Emerging Ultra-Narrow-Band Cyan-Emitting Phosphor for White LEDs with Enhanced Color Rendition, *Light: Sci. Appl.*, 2019, **8**(1), 38, DOI: 10.1038/s41377-019-0148-8.
5 M.-Y. Qu, T.-Q. Li and Q.-L. Liu, Photoluminescence Properties of Cyan-Emitting $Lu_3Ga_xAl_{5-x}O_{12}$:Ce^{3+} Garnet Phosphors Synthesized in Nonreducing Atmosphere and at Different Temperature for High Quality w-LEDs, *Materials*, 2022, **15**(19), 6817, DOI: 10.3390/ma15196817.
6 X. Piao, K. Machida, T. Horikawa, H. Hanzawa, Y. Shimomura and N. Kijima, Preparation of CaAlSiN3:Eu2+ Phosphors by the Self-Propagating High-Temperature Synthesis and Their Luminescent Properties, *Chem. Mater.*, 2007, **19**(18), 4592–4599, DOI: 10.1021/cm070623c.
7 R.-J. Xie, N. Hirosaki, H.-L. Li, Y. Q. Li and M. Mitomo, Synthesis and Photoluminescence Properties of β-Sialon: Eu2+ (Si6−zAlzOzN8−Z:Eu2+): A Promising Green Oxynitride Phosphor for White Light-Emitting Diodes, *J. Electrochem. Soc.*, 2007, **154**(10), J314, DOI: 10.1149/1.2768289.
8 K. Park, T. Kim, Y. Yu, K. Seo and J. Kim, Y/Gd-Free Yellow $Lu_3Al_5O_{12}$:Ce^{3+} Phosphor for White LEDs, *J. Lumin.*, 2016, **173**, 159–164, DOI: 10.1016/j.jlumin.2016.01.014.
9 K.-B. Kim, Y.-I. Kim, H.-G. Chun, T.-Y. Cho, J.-S. Jung and J.-G. Kang, Structural and Optical Properties of BaMgAl 10O17:Eu2+ Phosphor, *Chem. Mater.*, 2002, **14**(12), 5045–5052, DOI: 10.1021/cm020592f.
10 S. Wang, Z. Song and Q. Liu, Recent progress in Ce^{3+}/Eu^{2+}-activated LEDs and persistent phosphors: focusing on the local structure and the electronic structure, *J. Mater. Chem. C*, 2023, **11**, 48–96, DOI: 10.1039/D2TC02639B.
11 G. Li, Y. Tian, Y. Zhao and J. Lin, Recent Progress in Luminescence Tuning of Ce^{3+} and Eu^{2+}-Activated Phosphors for Pc-WLEDs, *Chem. Soc. Rev.*, 2015, **44**(23), 8688–8713, DOI: 10.1039/C4CS00446A.
12 L. G. V. Uitert, Characterization of Energy Transfer Interactions between Rare Earth Ions, *J. Electrochem. Soc.*, 1967, **114**(10), 1048, DOI: 10.1149/1.2424184.
13 C. K. Jørgensen, Fractional Charges, Integral Oxidation States and the Nephelauxetic Effect in the Five Transition Groups, *Helv. Chim. Acta*, 1967, **50**(S1), 131–146, DOI: 10.1002/hlca.19670500911.
14 P. Dorenbos, The Nephelauxetic Effect on the Electron Binding Energy in the 4f Ground State of Lanthanides in Compounds, *J. Lumin.*, 2019, **214**, 116536, DOI: 10.1016/j.jlumin.2019.116536.
15 P. Dorenbos, Lanthanide 4f-Electron Binding Energies and the Nephelauxetic Effect in Wide Band Gap Compounds, *J. Lumin.*, 2013, **136**, 122–129, DOI: 10.1016/j.jlumin.2012.11.030.
16 A. L. Tchougréeff and R. Dronskowski, Nephelauxetic Effect Revisited, *Int. J. Quantum Chem.*, 2009, **109**(11), 2606–2621, DOI: 10.1002/qua.21989.
17 P. Dorenbos, Crystal Field Splitting of Lanthanide $4f^{n-1}5d$-Levels in Inorganic Compounds, *J. Alloys Compd.*, 2002, **341**(1), 156–159, DOI: 10.1016/S0925-8388(02)00056-7.
18 P. Dorenbos, 5d-level energies of and the crystalline environment. III. Oxides containing ionic complexes, *Phys. Rev. B: Condens. Matter Mater. Phys.*, 2001, **64**, 125117, DOI: 10.1103/PhysRevB.64.125117.
19 P. Dorenbos, 5d-Level Energies of Ce^{3+} and the Crystalline Environment. IV. Aluminates and "Simple" Oxides, *J. Lumin.*, 2002, **99**(3), 283–299, DOI: 10.1016/S0022-2313(02)00347-2.
20 J. Qiao, D. Li, Q. Shi, H. Guo, P. Huang and L. Wang, Compositional Engineering of Phase-Stable and Highly Efficient Deep-Red Emitting Phosphor for Advanced Plant Lighting Systems, *Light: Sci. Appl.*, 2024, **13**(1), 319, DOI: 10.1038/s41377-024-01679-9.
21 S. Hariyani, M. Sójka, A. Setlur and J. Brgoch, A Guide to Comprehensive Phosphor Discovery for Solid-State

Lighting, *Nat. Rev. Mater.*, 2023, **8**(11), 759–775, DOI: 10.1038/s41578-023-00605-6.

22 T. Takeda, R.-J. Xie, T. Suehiro and N. Hirosaki, Nitride and Oxynitride Phosphors for White LEDs: Synthesis, New Phosphor Discovery, Crystal Structure, *Prog. Solid State Chem.*, 2018, **51**, 41–51, DOI: 10.1016/j.progsolidstchem.2017.11.002.

23 R.-J. Xie and N. Hirosaki, Silicon-Based Oxynitride and Nitride Phosphors for White LEDs—A Review, *Sci. Technol. Adv. Mater.*, 2007, **8**, 588, DOI: 10.1016/j.stam.2007.08.005.

24 J. Sokolnicki, Nitridated $CaSiO_3$:Eu^{2+} and $SrSiO_3$:Eu^{2+} Phosphors for LEDs, *J. Alloys Compd.*, 2022, **903**, 163973, DOI: 10.1016/j.jallcom.2022.163973.

25 R. M. Pritzl, M. M. Pointner, K. Witthaut, P. Strobel, P. J. Schmidt and W. Schnick, Tunable Narrow-Band Cyan-Emission of Eu^{2+}-Doped Nitridomagnesophosphates $Ba_{3-x}Sr_x[Mg_2P_{10}N_{20}]$:$Eu^{2+}$ (x = 0–3), *Angew. Chem., Int. Ed.*, 2024, **63**(23), e202403648, DOI: 10.1002/anie.202403648.

26 H.-L. Li, R.-J. Xie, N. Hirosaki and Y. Yajima, Synthesis and Photoluminescence Properties of $Sr_2Si_5N_8$:Eu^{2+} Red Phosphor by a Gas-Reduction and Nitridation Method, *J. Electrochem. Soc.*, 2008, **155**(12), J378, DOI: 10.1149/1.2999278.

27 Y. Q. Li, A. C. A. Delsing, R. Metslaar, G. de With and H. T. Hintzen, Photoluminescence Properties of Rare-Earth Activated $BaSi_7N_{10}$, *J. Alloys Compd.*, 2009, **487**(1), 28–33, DOI: 10.1016/j.jallcom.2009.08.019.

28 N. Lee, J. Zeler, M. Sójka, E. Zych and J. Brgoch, Modulating Optical Properties through Cation Substitution: Composition-Property Relationships in MI3MIIIP$_3$O$_9$N:Eu^{2+} (MI = Na, K; MIII = Al, Ga, In), *Inorg. Chem. Front.*, 2025, DOI: 10.1039/D5QI00410A.

29 S. Hariyani, X. Xing, M. Amachraa, J. Bao, S. P. Ong and J. Brgoch, Realizing Wide-Gamut Human-Centric Display Lighting with $K_3AlP_3O_9N$:Eu_{2+}. Adv, *Opt. Mater.*, 2023, **11**(8), 2202689, DOI: 10.1002/adom.202202689.

30 J. Alkemper and H. Fuess, The Crystal Structures of $NaMgPO_4$, $Na_2CaMg(PO_4)_2$ and $Na_{18}Ca_{13}Mg_5(PO_4)_{18}$: New Examples for Glaserite Related Structures, *Z. Kristallogr. Cryst. Mater.*, 1998, **213**(5), 282–287, DOI: 10.1524/zkri.1998.213.5.282.

31 J. Wang, B. H. Toby, P. L. Lee, L. Ribaud, S. M. Antao, C. Kurtz, M. Ramanathan, R. B. Von Dreele and M. A. Beno, A Dedicated Powder Diffraction Beamline at the Advanced Photon Source: Commissioning and Early Operational Results, *Rev. Sci. Instrum.*, 2008, **79**(8), 085105, DOI: 10.1063/1.2969260.

32 B. H. Toby and R. B. Von Dreele, GSAS-II: The Genesis of a Modern Open-Source All Purpose Crystallography Software Package, *J. Appl. Cryst.*, 2013, **46**(2), 544–549, DOI: 10.1107/S0021889813003531.

33 K. Momma and F. Izumi, VESTA 3 for Three-Dimensional Visualization of Crystal, Volumetric and Morphology Data, *J. Appl. Cryst.*, 2011, **44**(6), 1272–1276, DOI: 10.1107/S0021889811038970.

34 J. C. de Mello, H. F. Wittmann and R. H. Friend, An Improved Experimental Determination of External Photoluminescence Quantum Efficiency, *Adv. Mater.*, 1997, **9**(3), 230–232, DOI: 10.1002/adma.19970090308.

35 V. F. Sears, Neutron Scattering Lengths and Cross Sections, *Neutron News*, 1992, **3**(3), 26–37, DOI: 10.1080/10448639208218770.

36 L. Pauling, The Nature of the Chemical Bond. IV. the Energy of Single Bonds and the Relative Electronegativity of Atoms, *J. Am. Chem. Soc.*, 1932, **54**(9), 3570–3582, DOI: 10.1021/ja01348a011.

37 M. L. Myrick, N. Simcock,Michael, M. Baranowski, H. Brooke, S. L. Morgan and J. N. McCutcheon, The Kubelka-Munk Diffuse Reflectance Formula Revisited, *Appl. Spectrosc. Rev.*, 2011, **46**(2), 140–165, DOI: 10.1080/05704928.2010.537004.

38 M. Pichler, J. Szlachetko, I. E. Castelli, N. Marzari, M. Döbeli, A. Wokaun, D. Pergolesi and T. Lippert, Determination of Conduction and Valence Band Electronic Structure of LaTiON Thin Film, *ChemSusChem*, 2017, **10**(9), 2099–2106, DOI: 10.1002/cssc.201601632.

39 R. D. Shannon, Revised Effective Ionic Radii and Systematic Studies of Interatomic Distances in Halides and Chalcogenides, *Acta Crystallogr., Sect. A*, 1976, **32**(5), 751–767, DOI: 10.1107/S0567739476001551.

40 A. R. Denton and N. W. Ashcroft, Vegard's Law, *Phys. Rev. A*, 1991, **43**(6), 3161–3164, DOI: 10.1103/PhysRevA.43.3161.

41 L.-J. Yin, J. Dong, Y. Wang, B. Zhang, Z.-Y. Zhou, X. Jian, M. Wu, X. Xu, J. R. van Ommen and H. T. Hintzen, Enhanced Optical Performance of $BaMgAl_{10}O_{17}$:Eu^{2+} Phosphor by a Novel Method of Carbon Coating, *J. Phys. Chem. C*, 2016, **120**(4), 2355–2361, DOI: 10.1021/acs.jpcc.5b10215.

42 W.-Q. Liu, D. Wu, H. Chang, R.-X. Duan, W.-J. Wu, G. Amu, K.-F. Chao, F.-Q. Bao and O. Tegus, The Enhanced Red Emission and Improved Thermal Stability of $CaAlSiN_3$:Eu^{2+} Phosphors by Using Nano-EuB_6 as Raw Material, *Nanomaterials*, 2018, **8**(2), 66, DOI: 10.3390/nano8020066.

43 J. Qiao, S. Zhang, X. Zhou, W. Chen, R. Gautier and Z. Xia, Near-Infrared Light-Emitting Diodes Utilizing a Europium-Activated Calcium Oxide Phosphor with External Quantum Efficiency of up to 54.7%, *Adv. Mater.*, 2022, **34**(26), 2201887, DOI: 10.1002/adma.202201887.

44 J. Mooney and P. Kambhampati, Get the Basics Right: Jacobian Conversion of Wavelength and Energy Scales for Quantitative Analysis of Emission Spectra, *J. Phys. Chem. Lett.*, 2013, **4**(19), 3316–3318, DOI: 10.1021/jz401508t.

45 N. Bardsley and B. Consulting, *Department of Energy*, 2022, *Solid-State Lighting R&D Opportunities*, https://www.energy.gov/eere/ssl/articles/doe-publishes-2022-solid-state-lighting-rd-opportunities.

46 D. L. MacAdam, Visual Sensitivities to Color Differences in Daylight, *J. Opt. Soc. Am.*, 1942, **32**(5), 247–274, DOI: 10.1364/JOSA.32.000247.

47 M. Sójka, S. Hariyani, N. Lee and J. Brgoch, Colossal Chromatic Shift in the $Ba_2Ca_2B_4O_{10}$:Ce^{3+} Phosphor, *Chem. Mater.*, 2023, **35**, 6491–6501, DOI: 10.1021/acs.chemmater.3c01465.

48 J. Zhong, W. Zhao, Y. Zhuo, C. Yan, J. Wen and J. Brgoch, Understanding the Blue-Emitting Orthoborate Phosphor $NaBaBO_3$:Ce^{3+} through Experiment and Computation, *J. Mater. Chem. C*, 2019, **7**(3), 654–662, DOI: 10.1039/C8TC05629C.

